Materials & Design 231 (2023) 112020

Contents lists available at ScienceDirect

Materials & Design

journal homepage: www.elsevier.com/locate/matdes

Effect of laser-induced groove morphology on the wettability and performance of Lithium-ion batteries

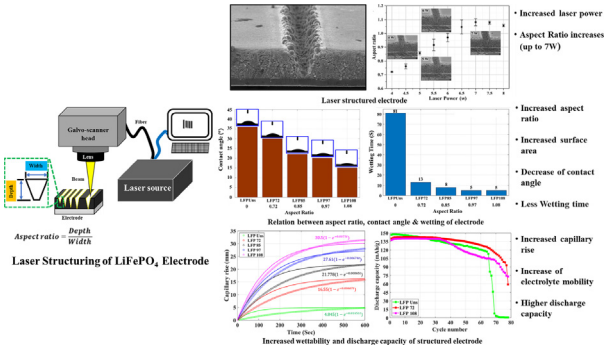
Mulugeta Gebrekiros Berhe [a,g], Hong Geun Oh [b], Seung-Keun Park [b], Mounarik Mondal [d], Dongkyoung Lee [c,d,e,f,1,*]

[a] MaPS - Department of Mechanical Engineering, KU Leuven, Leuven, Belgium
[b] Department of Advanced Materials Engineering, Chung-Ang University, Anseong, South Korea
[c] Department of Future Convergence Engineering, Cheonan College of Engineering, Kongju National University, Cheonan, South Korea
[d] Department of Mechanical and Automotive Engineering, Cheonan College of Engineering, Kongju National University, Cheonan, South Korea
[e] Center for Advanced Powder Materials and Parts of Powder (CAMP^2), Cheonan College of Engineering, Kongju National University, Cheonan, South Korea
[f] Global Institute of Manufacturing Technology (GITECH), Kongju National University, Cheonan, South Korea
[g] Flanders Make, KU Leuven, Leuven, Belgium

HIGHLIGHTS

- Laser structuring of $LiFePO_4$ electrode material.
- Effect of the aspect ratio of structured electrodes on wettability and its comparison with unstructured electrodes.
- Comparative study of wetting rate with the capillary rise and wetting balance test between structured and Unstructured electrodes.
- Usage and comparison of Lucas Washburn model and Zhmud extended model for quantifying the wetting rate.
- Electrochemical analysis for cyclic stability, rate capability, and charge–discharge profile.

GRAPHICAL ABSTRACT



ARTICLE INFO

Article history:
Received 20 December 2022
Revised 18 May 2023
Accepted 19 May 2023
Available online 27 May 2023

Keywords:
Laser structuring
3D electrode
Aspect-ratio

ABSTRACT

Lithium-ion batteries are widely used for their high energy density, high power density, long lifetime, and safety which are crucial for the environmentally friendly future energy system. Electrodes are the key component of LIBs that determines battery performance. $LiFePO_4$ is a common electrode used in battery technology due to its long cycle life and good safety. Laser structuring of electrodes has recently been considered a promising approach to increase energy density. In this work, $LiFePO_4$ electrodes were structured into a grid-type pattern by varying the laser power, resulting in different aspect ratios. To evaluate the effects of the structuring, wettability and electrochemical performance were tested. The wetting property was investigated using spread area, wetting time, and contact angle measurements. Besides, the wetting rate was measured using the wetting balance test and capillary rise test. Lucas Washburn

* Corresponding author at: Department of Mechanical and Automotive Engineering, Cheonan College of Engineering, Kongju National University, Cheonan, 31080, South Korea.
E-mail address: ldkkinka@kongju.ac.kr (D. Lee).
[1] This research was performed while Mulugeta Gebrekiros Berhe was at Department of Future Convergence Engineering, Cheonan College of Engineering, Kongju National University, Cheonan, South Korea.

https://doi.org/10.1016/j.matdes.2023.112020
0264-1275/© 2023 The Author(s). Published by Elsevier Ltd.
This is an open access article under the CC BY license (http://creativecommons.org/licenses/by/4.0/).

Wettability
Battery performance

model and Zhmud extended model were used to quantitatively express the wetting rate. The influence of gravity on the wetting performance was also investigated by comparing those models. Furthermore, an electrochemical test was performed to see the cyclic stability, rate capability, and charge–discharge profile with a C rate up to 1C.

© 2023 The Author(s). Published by Elsevier Ltd. This is an open access article under the CC BY license (http://creativecommons.org/licenses/by/4.0/).

1. Introduction

Recently Lithium-ion battery (LIB) technology has become very important as modern civilization has become mainly dependent on fossil fuels. But, the use of fossil fuels is followed by two serious difficulties, which are the opposition of countries to fossil fuels and CO_2 emissions. Moreover, they primarily result in global warming [1,2]. LIBs are the most widely used battery for portable electronics, electric vehicles, power tools, and various electric grid applications due to their high power and energy densities, less cost, and better life cycle [1–5]. As LIBs' energy density is mainly determined by their output voltage and specific capacity, this makes electrodes a very essential component. The electrode component of LIBs is composed of the active material and current collector with a large surface area for the electrochemical process during the charging and discharging cycle [6,7].

To meet the rapidly growing customer requirements of the electronic vehicle industry, further performance development of LIBs is essential in terms of energy and power densities. Most researchers have focused on improving material characteristics and chemical composition, increasing electrode thickness and increasing the mass loading (amount of active material per area) [5,6]. However, other than mass loading, most of these concepts would inevitably increase the manufacturing cost and complexity of the process as well as increase cell resistance. Moreover, increasing the thickness of the electrode with high active material loading may lead to decrease in average discharge voltages, solid phase and electrolyte lithium-ion concentration [6–10].

There are several other techniques that have been employed to improve energy and power density such as co-extrusion, freeze cast, layered structure.Recently applying laser technology in this field to generate three-dimensional (3D) architectures has shown a promising approach [46]. This idea shortens the lithium transport path, improving lithium-ion diffusion kinetics and increasing power density [11–16]. Areal energy capacity can also be enhanced by the concept of 3D battery electrode architecture while at the same time maintaining high power densities [9]. Moreover, increasing the wettability of electrodes, enhances pore filling duration [17]. The wetting behavior influence is not only limited to the battery performance but also it affects the LIBs production process. It helps in facilitating the most time-consuming electrolyte filling and wetting process. Therefore, it is essential to understand the relationship between electrode microstructure and electrolyte wetting of electrodes to accelerate this production process and enhance battery performance [18]. So far, the effect of the laser-modified 3D electrode on the wettability and electrochemical performance of the battery is significantly less reported. Moreover, the works of literature present less quantitative data about the wettability of electrodes and most of them don't consider the effect of gravitational force on the wetting behavior [17–21].

In recent works of Proll et al. and Mangang et al. [9,22], it is presented that laser structuring of an electrode leads to enhancement of LIB performance. Pfleging et al.[21] compared performance and wetting of unstructured and structured NMC electrodes. He reported that 3D architecture in thick electrodes improves the wettability and electrochemical cell operation of LIBs. The promising technology of laser structuring has shown to be a significant approach to stabilizing the capacity of different electrodes such as $LiCoO_2$ and $LiMn_2O_4$ as a result of the increased active surface area [23–26]. In another study, Pfleging [6] reported that the application of laser technology to structure thick electrode films resulted in an extended battery lifetime and increased capacity. He also realized the wettability of electrodes was improved after laser structuring. Besides the improved lithium-ion diffusion skinetics, an enormous wettability improvement is realized with 3D electrodes [8]. Pfleging [6] mentioned that the combination of complete electrolyte wetting and active surface area increment is vital for the overall LIBs' performance. In addition, the effect of porosity and thickness changes during calendaring has a significant impact on the electrode's pore structure, thereby influencing the wettability of the film [24]. However, past studies do not extensively present the effect of laser structured electrodes with different aspect ratios on wettability and electrochemical performance in detail. In addition, previous studies in this area mainly focused on line-type patterns with a limitation of detailed experimental works. The other most significant drawback seen in previous works is using the Lucas Washburn (LW) model, which neglects the effect of gravity. Choi et al. [40] investigated the wicking mechanism using the capillary rise test (CRT) and wetting balance test (WBT) approaches and compared them with analytical models. Benltoufa et al. [41] studied the wetting parameters of jersey knitting textile material using the LW equation. Pfleging et al. [21] studied the wetting rates of unstructured and structured electrodes from the CRT results. Zhmud et al. [26] presented the mathematical model considering gravity, and Fries et al. [27] extended Zhmud's solution into its exact form.

In the present work, a nanosecond pulsed laser was used to generate 3D grid patterns over the surface of Lithium iron phosphate ($LiFePO_4$, LFP) electrodes. In the category of ultra-short, pulsed lasers other than a nanosecond(NS) lasers, both picosecond(PS) lasers and femtosecond(FS) lasers are incredibly costly. Thus, in this work, attempts are made to carry out laser structuring on LFP with Ns lasers with an aim to generate a good wettable surface while simultaneously providing economic benefits. Post-laser processing features are reported in terms of ablation depth, width, aspect ratio, and the change in material atomic concentration. Contact angle, spread area, wetting time, and wetting rate measurements were used to determine the wetting behavior of the unstructured and structured electrodes. Furthermore, the wetting rate is examined from the WBT and CRT using LW and extended models proposed by Zhmud et al. [26] and Fries et al. [27]. The electrochemical performance was also probed using the charge–discharge profile, rate capability, and cyclic stability.

2. Experimental

2.1. Material

The commercial LFP electrode and $LiPF_6$ electrolyte used in this study were manufactured by MTI Corporation. The LFP particle size was 10 μm. The single-side carbon coated LFP has a total thickness of 83 μm with 68 μm thick active material, and a 15 μm thick aluminum current collector. The electrode is composed of 91 wt% LFP

active material and the remaining 9 %wt was assigned to the combination of PVDF binder (5%) and conductive carbon black(4%). The electrolyte solution is 1:1 (volumetric ratio) EC: EMC with 1 M $LiPF_6$.

2.2. Laser structuring

A nanosecond fiber laser (YLPM-1–4 × 200–20-20, IPG Phonetics Corporation) operating at a wavelength of 1064 nm and a working distance of 189 mm was used to produce the grid type 3D electrode with a pitch distance of 200μ m between each groove. Laser structuring was performed with laser power in the range of 4 – 8 W. The laser pulse duration and scanning speed were set to 4 ns and 1500 mm/s, respectively, aiming to reduce the thermal effects. A repetition rate of 1000 kHz and three passes were also employed to fabricate the grooves. The focus diameter of the laser beam was 30μ m. A detailed description of the laser machine used for this work can be found elsewhere [24]. The laser parameters used for the experiment are given in Table 1 and the experimental setup used can be seen in Fig. 1.

2.3. Morphology and wetting properties

Scanning electron microscopy (SEM) was used to investigate the geometry changes such as ablation width and ablation depth in addition to the electrode morphology. The spread area of electrolytes over the electrodes was examined using an optical microscope, whereas a contact angle analyzer (Phoenix300 tourch 140318) was used for measuring the static contact angles. The wetting time was measured during this experiment only using 8 μl of electrolyte. The capillary rise was examined by measuring the height of the liquid rise in a vertical direction. The capillary rises and wetting balance methods were conducted on a 50 × 20 (l × b) mm electrode sample size [28,30]. The porous electrode sample was immersed in the electrolyte container. The electrolyte starts rising into the capillary groove structure until it reaches the saturation or equilibrium height, and then the sample was withdrawn. The wetting balance method (gravimetric method) was applied to track the sample mass of liquid infiltrating the electrode sample [29]. The sample was held down from above, and a container with liquid electrolyte was lifted to immerse the sample to a depth of 10 mm. The details of this setup are explained in Fig. 2.

2.4. Battery performance test

An electrochemical test of the unstructured and structured electrodes was performed using WBCS3000L (Wonatech, Korea) in a 2032-type coin cell. Lithium-metal foils were employed as opposite electrodes in the coin cell with a diameter of 11 mm, and a glass filter was used as the separator. The electrolyte was composed of 1 M $LiPF_6$ dissolved in EC/DEC with a volume ratio of 1:1 was used. The charge and discharge cycles were carried out enhancing the current rate from 0.1 to 1C and the voltage range between 2.5 and 4.2 V.

3. Theoretical background

The momentum balance equation describes the liquid flow in the capillary with assumptions such as (a) the flow is one-dimensional (b) no entry effects or inertia in the liquid container (c) the displaced air does not cause any inertia or friction effects (d) the pressure loss due to viscosity is given by Hagen-Poiseuille [29,30]. Considering the first assumption, the vertical surface tension is in charge of lifting the liquid straight up which means the horizontal surface tension is ignored. The momentum balance equation is described as (Fig. 3):

Table 1
Laser parameters used for the experiment.

Laser parameters	
Laser power	4–8 W
Pulse duration	4 ns
Repetition rate	1000 kHz
Scanning speed	1500 mm/s
Number of passes	3
Pitch distance	200 μm

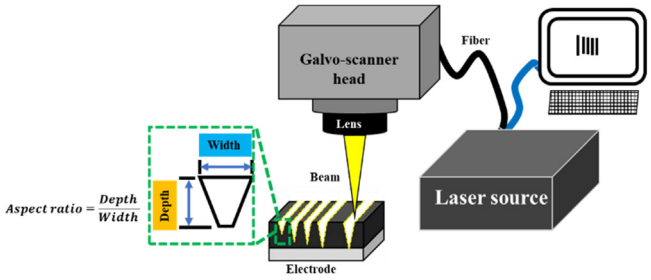


Fig. 1. Set up for laser structuring of electrodes.

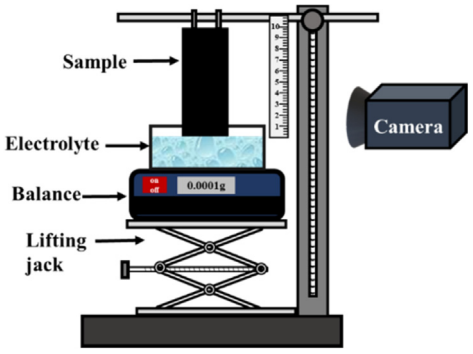


Fig. 2. Experimental setup for capillary rise and wetting balance tests.

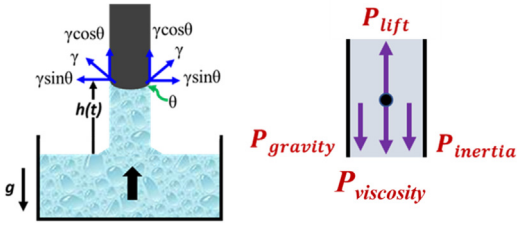


Fig. 3. Vertical capillary rise setup.

$$P_{lift} = P_{gravity} + P_{viscosity} + P_{inertia} \quad (1)$$

$$\frac{2\gamma\cos\theta}{R} = \rho g h + \frac{8\mu h}{R^2}\dot{h} + \rho\frac{d(h\dot{h})}{d(t)} \quad (2)$$

where, P_{lift} is the capillary pressure which drives the liquid upward, $P_{gravity}$ is the gravity term, $P_{viscosity}$ and $P_{inertia}$ are the pressure losses due to viscosity (given by Hagen-Poiseuille) and inertia, consecutively. γ represents the surface tension, θ is the contact angle, R is the capillary radius, ρ is the fluid density, μ refers to the viscosity of the liquid and h is the capillary rise height at the time, t. Remind-

ing the assumption that there is no inertia or entry effect in the liquid reservoir, Equation (2) can be refined to

$$\frac{8\mu h}{R^2}\dot{h} = \frac{2\gamma\cos\theta}{R} - \rho g h \tag{3}$$

$$\frac{dh}{dt} = \frac{R^2}{8\mu h}\left(\frac{2\gamma\cos\theta}{R} - \rho g h\right) \tag{4}$$

When gravity is ignored according to LW, Equation (4) can be further reduced to the following

$$\frac{dh}{dt} = \frac{R\gamma\cos\theta}{4\mu h} \tag{5}$$

Integrating the ordinary differential equation and applying the initial conditions t = 0 and h = 0 leads to the final form of the LW equation which is given as

$$h = k\sqrt{t},\ k = P\sqrt{\frac{R\gamma\cos\theta}{2\mu}} \tag{6}$$

where k is the wetting rate and refers to the penetration ability of the liquid. The wetting rate is used to quantitatively compare wetting behavior for electrodes and other porous materials where liquid infiltration is undergoing. A higher value of this term indicates that the wetting is faster on the porous surface [26].

$$h = \frac{\Delta m}{\rho . A_e} \tag{7}$$

$$\frac{\Delta m}{\rho . A_e} = k\sqrt{t} + b \tag{8}$$

Equation (6) can be again described by the modified LW equation. Using this modified equation capillary rise height can be expressed in terms of electrode cross-section area (A_e) and density of the liquid (ρ). b is the mass correction factor.

However, the LW equation is not applied when the influence of gravity is significant. Fries et al. [24,30] showed that the LW equation can only be used to predict data up to 10–20% of the equilibrium height (h_{eq}). Above 10–20% of the equilibrium height, the effect of gravity cannot be neglected as it becomes very significant. The equilibrium height is where the upward capillary and downward gravity forces are balanced. It is also known as saturation height and can be calculated as the following

$$h_{eq} = \frac{2\gamma\cos\theta}{R\rho g} \tag{9}$$

Due to the drawback of the LW equation, Zhmud et al. [22] showed the so-called extended model taking gravity into account. The extended model can be expressed by recalling Equation (3)

$$\frac{dh}{dt} = \frac{R^2}{8\mu h}\left(\frac{2\gamma\cos\theta}{R} - \rho g h\right) \tag{10}$$

$$\frac{dh}{dt} = \left(\frac{R\gamma\cos\theta}{4\mu h} - \frac{\rho g R^2}{8\mu}\right) \tag{11}$$

To reduce the complexity of the above equation, constants a and b are introduced as

$$a = \frac{R\gamma\cos\theta}{4\mu}\ and\ b = \frac{\rho g R^2}{8\mu} \tag{12}$$

Rewriting Equation (11) gives

$$\frac{dh}{dt} = \left(\frac{a}{h} - b\right) \tag{13}$$

The analytical solution for this ordinary differential equation is given as

$$t = -\frac{h}{b} - \frac{a}{b^2}\ln(bh - a) \tag{14}$$

Zhmud et al. [22] generated a long-term asymptotic solution as shown below.

$$h(t) = \frac{a}{b}(1 - e^{-\frac{b^2 t}{a}}) \tag{15}$$

The wetting rate discussed above can be expressed using the following relation in the extended model.

$$k = \sqrt{2a} \tag{16}$$

However, Fries et al. [23,28] obtained an accurate solution from Equation (14) in terms of h(t). Equation (14) was multiplied by $-\frac{b^2}{a}$ both sides followed by taking off power e each side to give

$$e^{-1-\frac{b^2 t}{a}} = (a - bh)e^{(\frac{hb}{a}-1)} \tag{17}$$

To obtain a simplified formula for finding out 'h', Lambert W function [33] was used as shown in equation (18). To reach the desired form in equation (18) both sides of the equation (17) was divided by 'a' and a negative sign was taken out which resulted to a new equation (19)

$$x = W(x)e^{W(x)} \tag{18}$$

$$\frac{e^{-1-\frac{b^2 t}{a}}}{a} = \left(\frac{hb}{a} - 1\right)e^{(\frac{hb}{a}-1)} \tag{19}$$

Equation (19) is now of the form $y = ze^z$ and according to Lambert W function we can write, if $z = w(y)$ hence we can re write equation (19) in the form as shown in equation (20) [29]

$$\frac{hb}{a} - 1 = w\left(\frac{-e^{-1-\frac{b^2 t}{a}}}{a}\right) \tag{20}$$

Further, simplifying this equation a relation of 'h' can be obtained

$$h(t) = \frac{a}{b}\left[1 + W\left(\frac{-e^{-1-\frac{b^2 t}{a}}}{a}\right)\right] \tag{21}$$

4. Result and discussion

4.1. Laser parameter study

The experimental was employed to achieve grooves with different aspect ratios. The ablation top width, bottom width, depth, and aspect ratio studied for different laser powers are shown in Fig. 4. The melt formation observed with increasing laser power is also depicted in Fig. 4. Both the ablation width and depth increase linearly as the laser power increases. Using the laser power of 8 W, an ablation width of 56μ m and an ablation depth of 59μ m were measured. None of the experimental laser powers completely removed the 68μ m thick LFP active material. Regarding aspect ratio, the laser power of 7 W resulted in a maximum aspect ratio of 1.08, which enhances the active electrode surface area [34]. The aspect ratio starts to decrease when the laser power greater than 7 W is applied. This behavior is due to the increment rate of width being more than that of depth. Absorbed laser energy increases the temperature, melting, and vaporization of material [35]. The effect of this phenomenon was well noticed as the laser power increased. Moreover, the formation of re-solidified molten material was noticed to large extent on both sides of the top edge of the groove. This is mainly because the melted active material

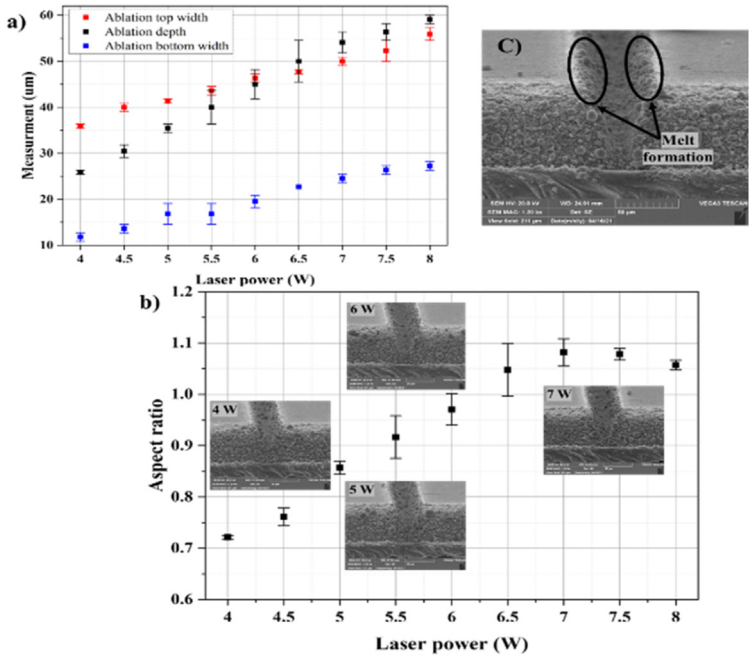


Fig. 4. (a) Ablation depth and width, (b) Aspect ratio, (c) SEM image of electrode structured with 8 W.

couldn't escape the deep groove and is trapped in the narrow top width.

The samples with a high aspect ratio (7 W) and low aspect ratio (4 W) and laser powers of 5 W and 6 W were chosen for further study. They are represented by using the name of the electrode material and their respective aspect ratios, such as LFP108, LFP97, LFP85, and LFP72. Similarly, the unstructured electrode is denoted as LFPUns. The samples are used to show the effect of groove morphology on the wettability and electrochemical performance of electrodes. When closely observed under the SEM, all the structured electrodes exhibited no defects due to irradiation of nano second lasers. Hence further testing of the wettability was carried out.

4.2. Wettability test

4.2.1. Spread area, wetting time, and contact angle

The samples for wettability test were prepared in a grid type pattern with 200μ m pitch distance between the grooves. Spread area, wetting time, contact angle, and wetting rate measurements are used to investigate the wettability of unstructured and structured electrodes. The spread area of electrolytes over the surface of electrode samples at six different time taken by the optical microscope is shown in Fig. 5 [27]. A 5 μl electrolyte was dropped in the middle of the electrode surface. The theoretical assumption that the pore distribution over the electrode surface is uniform is proved in this experiment, that majority of the sample's imbibition is symmetrical around the center [36]. The significant effect of laser structuring can be distinguished from the improved electrolyte spread area over the electrode surfaces. A wider spread area is seen in the sample LFP108, while the LFPUns electrode possessed a smaller spread area than other samples [27]. No notable change in the spread area was observed after reaching 80 sec for all samples, despite that the electrolyte in some samples started evaporating.

Fig. 6 illustrates the average wetting time required for the electrolyte to fully penetrate the electrode surface. The apparent effect of the laser-produced grooves can be seen in these measurements. A fast wettability is observed in LFP97 and LFP108 where the

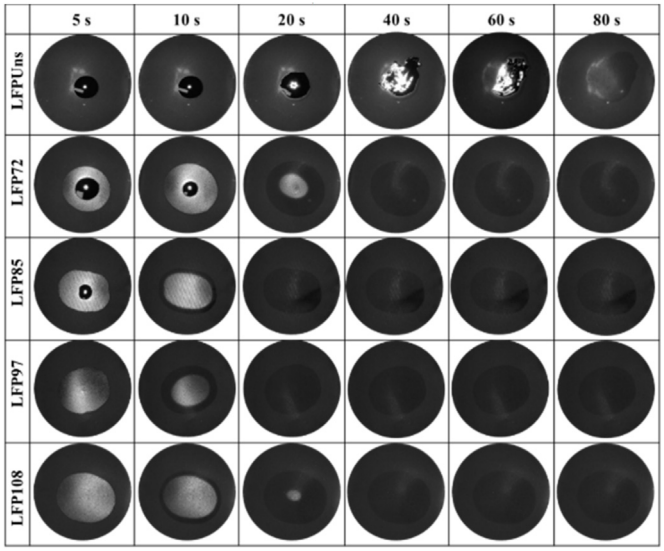


Fig. 5. Optical image for the spreading process of electrolyte.

electrolyte fully penetrates in 5 Sec. However, LFPUns show poor wetting time compared to the other laser-structured samples taking about 81 sec to absorb the electrolyte drop. Considering the standard deviation, no significant difference can be observed in the wetting time of the last three laser-structured samples (LFP72, LFP85, and LFP97).

The static contact angle between the electrode and electrolyte was measured to indicate the wettability corresponding to surface microstructure as shown in Fig. 7. The laser surface modification of electrodes leads to a remarkable decrease in contact angle from 36° to 15°. The LFPUns and LFP108 have the highest ($\theta = 36^{\circ}$) and smallest ($\theta = 15^{\circ}$) contact angles, respectively. It is expected that the laser irradiation on the surface of the electrodes has altered the surface roughness, and energy of the electrode alternating the acted upon surface tension between electrode and

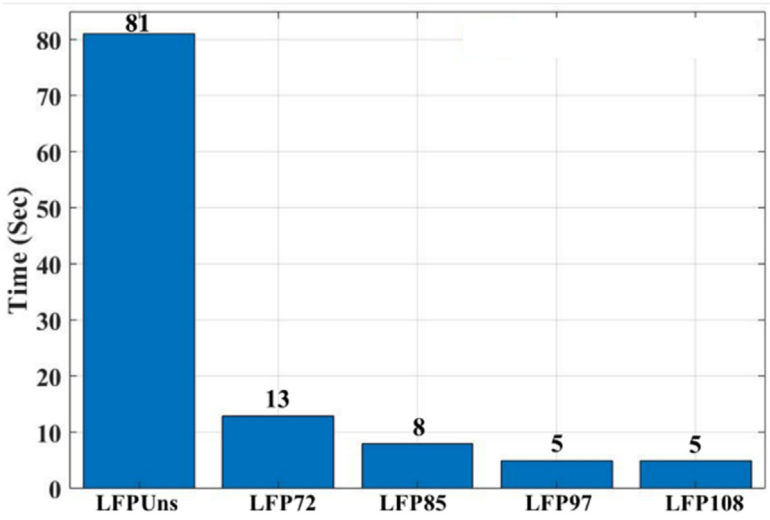


Fig. 6. Wetting time.

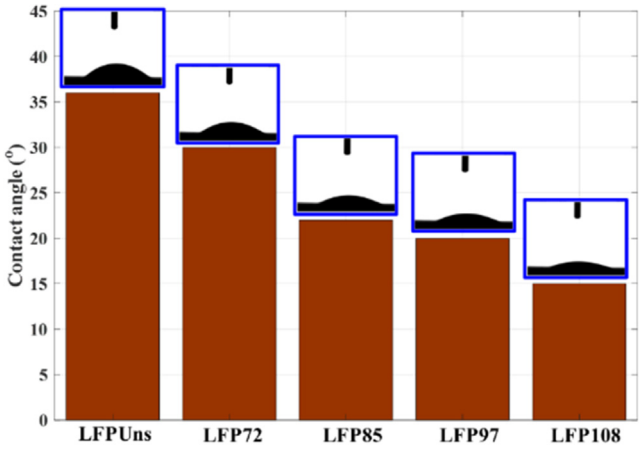


Fig. 7. Static contact angle measurements.

electrolyte [51,52]. A High contact angle represents poor wettability due to the high surface tension (resistance to penetration) between the electrode surface and the electrolyte. In addition to facilitating lithium-ion transfer, it is speculated that the structured electrode will reduce the amount of dry parts present in electrode. It is reported in literature that these dry parts in electrodes promote cell degradation due to inhomogeneous current distribution [20].

4.2.2. Capillary rise and wetting balance test

The active material on the electrode is modeled as a porous medium with capillary-type tubes, and the wetting process is driven by capillary force [37]. LW proposed a model of fluid movement in a capillary based on the momentum balance of resisting forces (inertia, gravity, and viscosity) and capillary driving force. The influence of gravity and inertia was neglected by LW for simplification. The details of the equation are explained in the theoretical analysis section.

By applying the material properties given in Table 2 [21], it is possible to develop the analytical models.

The other two terms, radius, R, and contact angle, θ have to be seen differently for the unstructured and structured samples. Recalling the concept that porous electrodes are composed of bundled capillary tubes, the pore radius is used as R. This is measured

Table 2
Material Properties for electrolyte.

γ [kg.s^{-2}]	ρ [kg.m^3]	μ[Pa.s]
0.0303	1500	0.00338

by Matlab image processing techniques using the watershed segmentation algorithm, an alternative to mercury intrusion porosimetry as shown in Fig. 8 [30,35]. The pore size distribution features some fluctuation, so a single average radius is used. The pore radius measured using this method is 3.5μ m.

Whereas, in the case of structured electrodes, the capillary radius R can be calculated as follows [37,38].

$$R = \frac{A_c}{P_w} \tag{22}$$

where $P_w(P_w = b + 2d\sqrt{1+m^2})$ is the wetting perimeter and A_c $(A_c = (b + md)d)$is the groove cross-sectional area (see Fig. 9).

The capillary radius for LFP72, LFP85, LFP97, and LFP108 are calculated as 11.3, 14.2, 16.76, and 18.77 um, respectively. Now it is possible to obtain the contact angle θ from Equation (9), which is obtained from the experiment. The equilibrium heights obtained from the experiment for LFPUns, LFP72, LFP85, LFP97, and LFP108 are 5.5, 17.36, 23.07, 29.23, and 32.3 mm, respectively. From this, contact angle of 89.7, 87.27, 85.43, 83.17, and 81.53° are derived for sample LFPUns, LFP72, LFP85, LFP97, and LFP108, respectively. Although Mercury porosimetry might be a good method for porosity measurement but other researchers mention using MATLAB's image processing techniques using the watershed segmentation algorithm. Further, this measurement is not closely associated with the goal of this study it is also believed that it would not affect the results severely. With all the combinations of calculated parameters and material properties indicated in Table 2, the analytical models for both LW and Zhmud extended models can be derived using Equations (6) and (15) as seen in Table 3 with their respective wetting rates. k_{A-LW} and $k_{A-Extended}$ represents wetting rates obtained from the analytical LW model and analytical extended model consecutively.

From these models, the wetting rates shown in Table 4 can be extracted using Equations (7) and (14).

There is no deviation between the wetting rates obtained from the analytical models despite being represented with different mathematical forms. However, the data from those two models

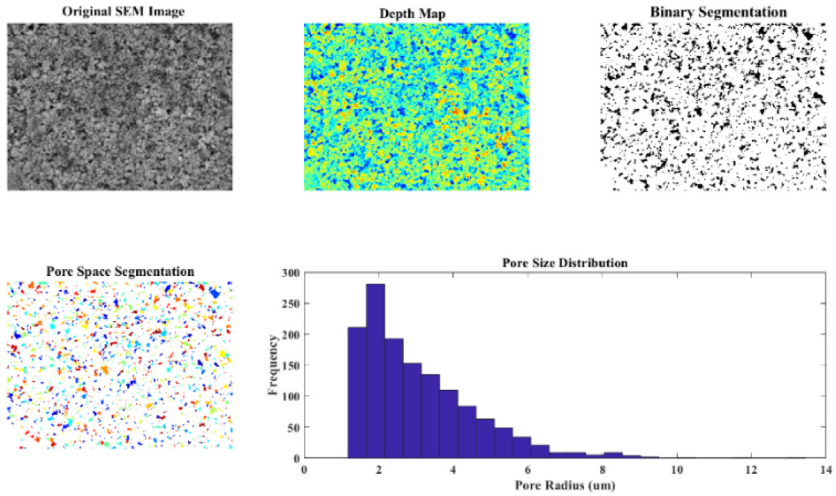


Fig. 8. Matlab-generated pore distribution.

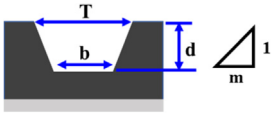


Fig. 9. Groove cross-sectional area.

Table 3
Analytical LW and extended models.

Sample	Analytical LW Model	Analytical Extended Model
LFPUns	$h(t) = 0.5\sqrt{t}$	$h(t) = 5.44\,(1 - e^{-3.25\times10^{-3}t})$
LFP72	$h(t) = 1.55\sqrt{t}$	$h(t) = 17.36\,(1 - e^{-4\times10^{-3}t})$
LFP85	$h(t) = 2.25\sqrt{t}$	$h(t) = 23.07\,(1 - e^{-4.75\times10^{-3}t})$
LFP97	$h(t) = 2.98\sqrt{t}$	$h(t) = 29.23\,(1 - e^{-5.22\times10^{-3}t})$
LFP108	$h(t) = 3.52\sqrt{t}$	$h(t) = 32.3(1 - e^{-5.93\times10^{-3}t})$

Table 4
Wetting rates from analytical solutions with respect to LW and extended models.

Sample	LFPUns	LFP72	LFP85	LFP97	LFP108
k_{A-LW}	0.5	1.55	2.25	2.98	3.52
$k_{A-Extended}$	0.5	1.55	2.25	2.98	3.52

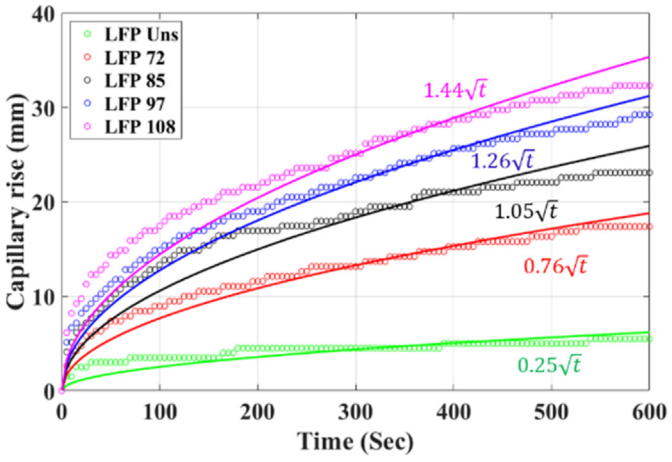


Fig. 10. CRT results with respect to the LW model.

have no agreement even though they share the same wetting rates. The groove geometry has affected the wetting rates obtained from the analytical models, as indicated in the results.

Fig. 10 shows the height versus time graph measured from the CRT for all samples. The wetting rate was determined for all samples from the h-t curve. The time-dependent capillary rise was investigated up to 600 Sec, where it nearly reaches saturation or equilibrium height.

The samples reached saturation height after about 600 Sec due to the balance between the driving capillary force and dragging gravity force. Time-dependent capillary rise and the wetting rates are dependent on the liquid electrolyte properties such as viscosity and surface tension in addition to electrode surface morphology. Sample LFP108 with a high aspect ratio has a superior wetting rate than the other samples. The LFPUns electrode has slower wetting, followed by samples LFP72, LFP85, and LFP97, respectively. The results from the fitting of the h-t curve show that the laser structuring has a clear effect on the capillary rise. In the sample with relatively poor wettability among the structured electrodes, the LFP72 improved the wetting property of the LFPUns by 68.2%. Whereas the sample LFP108 improved it by 83%. As discussed in the parameter study, the increase in the aspect ratio of capillaries (grooves) has contributed to the enhanced capillary rise height [37,39]. Not surprisingly the wetting speed is faster in the early stage than in the subsequent [16,21,34,36,39,40]. The wetting becomes slower as the time goes up and not much increase is noticed after it reaches the equilibrium or saturation height. This is because pores close to the electrolyte container serve as a reservoir for the unwetted region once they are saturated, making the wetting process slower with time [42]. The other reason is that for elongated time intervals, the effect of gravity becomes more dominant, which results in less wetting [29,40,42]. The presence of a solid-air interface due to the experimental setup may also be an additional cause. Moreover, the strong downward surface tension force generated due to the viscous resistance may have contributed to this phenomenon. It is realized that the electrolyte rising on the capillary structure shows a step rise increment in all the samples which may be because the pores vary periodically [39]. The linear equation of h-$\sqrt{t}$ determines the wetting rate discussed in Equation (6), by extracting the slope as stated by LW. The wetting rates values derived from the slope of the h-$\sqrt{t}$ are presented in Table 5.

The fitting of results to the LW equation is excellent, as verified by regression analysis (R^2 ranging from 89.93 to 99.26 %). The

Table 5
Wetting rates from CRT with respect to LW model.

Sample	LFPUns	LFP72	LFP85	LFP97	LFP108
k_{CRT-LW}	0.25	0.76	1.05	1.26	1.44

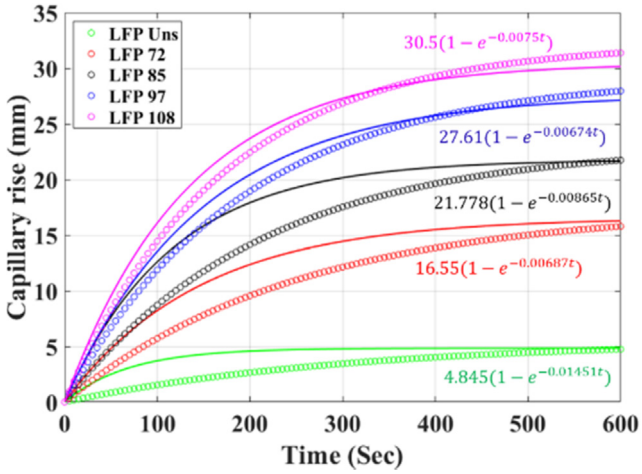


Fig. 11. CRT results with regard to the extended model.

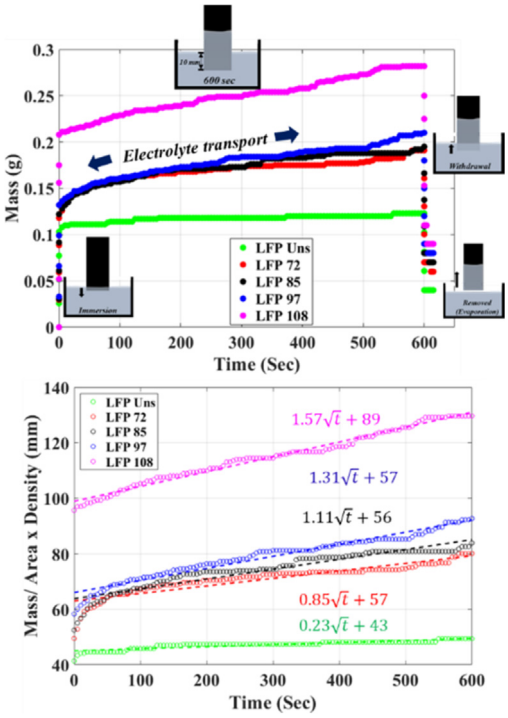


Fig. 12. A typical m-t curve and WBT results with regard to the LW model.

Table 6
Wetting rates from CRT with regard to the extended model.

Sample	LFPUns	LFP72	LFP85	LFP97	LFP108
$k_{CRT-Extended}$	0.82	1.93	2.8	3.2	3.7

Table 7
Wetting rates from WBT with regard to LW model.

Sample	LFPUns	LFP72	LFP85	LFP97	LFP108
k_{WBT-LW}	0.23	0.85	1.11	1.37	1.57

wetting rates from the analytical models are nearly double that of the wetting rates from the CRT concerning the LW model. The same data was used differently. The Zhmud extended model was used to process the data from CRT experimental results in order to obtain the wetting rate and mathematical model when gravity is taken into account. Fig. 11 and Table 6 illustrate this result. One can see that the first period of penetration deviates from the fitting and shows good agreement as time goes up. This suggests that the effect of gravity is more dominant for a long time and high potential rise. According to the results of the wetting rate showing the clear effect of groove morphology as the previous assessments, they are also close to the wetting rates obtained from the analytical models.

In a similar manner to the CRT measurement, the wetting rate can also be determined from the mass measurement approach known as the WBT [13,14,17,25,26,31,34,39,40]. Fig. 12 illustrates the measured absorbed mass of electrolyte with time from the WBT along with the extracted wetting rates in Table 7. As shown in Equation (8), the mass measurement is interpreted into height form. The resulting slope from this linearized graph determines the wetting rate, k.

This wetting balance test is advantageous over the capillary rise test to demonstrate wettability as it omits the necessity of video recordings [32]. The curve from mass measurement is divided into four categories as shown in the above figure [17,30]. Firstly, the electrode sample is inserted into the electrolyte container at high speed in the immersion phase. Next, the sample is left there with an immersion length of 10 mm inside the electrolyte, where the electrolyte is transported into the porous electrode. This region (absorption mass) is of great interest where the wetting rate and behavior can be evaluated. After keeping the sample in the electrolyte for 600 Sec, the sample is withdrawn at high speed, where it loses mass rapidly and then starts losing mass gradually due to evaporation after it is entirely removed. Tremendous and quick wetting takes place in the initial 0 to 2 Sec. Absorption mass is that significantly contributes to the acquired weight during the electrolyte transport. As can be seen from the above figures, the electrolyte mass absorbed by the sample LFP108 and LFPUns shows the maximum and minimum, respectively. A significant impact of laser structuring is noticed on the wettability according to the WBT result. However, the other samples LFP72, LFP85, and LFP97 did not experience big difference in the absorbed electrolyte mass. Quantitatively, it can be summarized from the mass versus time graph that the wettability increases as the sample groove's aspect ratio or capillary size increases. The average wetting rate for each sample are 0.23, 0.85, 1.11, 1.31, and 1.57 mm/s$^{0.5}$ in ascending order from LFPUns to LFP108 sample. The height data generated from the WBT result was also computed to determine the wetting rate when gravity is taken into account as shown in Fig. 13 and the wetting rates are given in Table 8.

As seen from the figure, the data and graph generated from the extended model fit of the result are exorbitant relative to the results from the other approaches. Yet comparing the effect of groove morphology quantitatively, the wetting rate results still expresses the superiority of LFP108 and poor behavior of LFPUns. The rest three samples show an insignificant difference in their wetting ability.

From Fig. 14, it can be seen that the LW analytical model shows a good fit with the experimental results in the early-stage time, and it deviates much as the time increases steadily. Whereas the analytical extended model shows good agreement and consistency with the experimental result indicating that the extended model can adequately handle the effect of gravity. Furthermore, looking at these three results (analytical LW, analytical extended, and CRT experiment), ignoring the gravity term, when assessing the wettability of material, may result in unreliable data even though the LW model is less complex and easier to apply. For the extended time, the LW model is not valid as the liquid flow velocity retards due to gravity as well as evaporation of the electrolyte due to its high evaporation rate by its nature [39,40]. The small deviation noticed between the experimental result and the analytical extended model indicates that gravity effect is less in the initial period than for elongated time. Because the effect of gravity increases as the potential of the capillary rise increase. It may also depend on the assumptions taken, such as the neglect of entry effects. Hence this small deviation also provides information that the boundary effect for wider capillaries was weaker than that of smaller ones [40]. Overall, the capillary rise and wetting balance tests demonstrate that the sample with maximum groove aspect ratio has stronger wettability. While the unstructured is poor swith its wetting behavior. One reason is that more amount of electrolytes can be sucked vertically in wider capillaries due to larger volume.

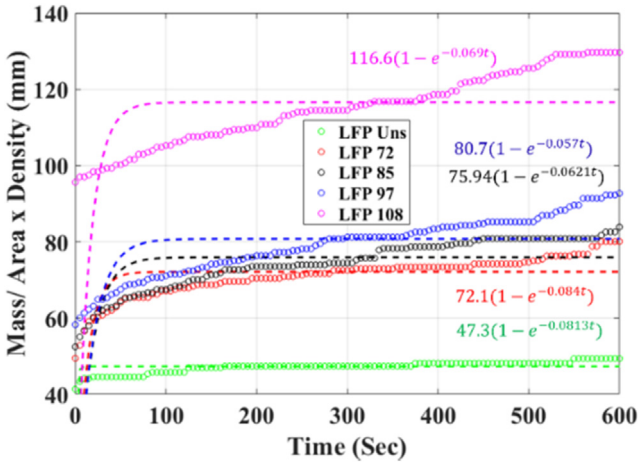


Fig. 13. WBT results with respect to the extended model.

Table 8
Wetting rates from WBT with regard to the extended model.

Sample	LFPUns	LFP72	LFP85	LFP97	LFP108
$k_{WBT-Extended}$	6.03	29.53	26.74	27.27	40.4

Consequently, electrolyte spreads more so that capillary rise height increases as witnessed in the discussed results. This leads to few boundary effects on the samples with larger width or capillary size. It has been stated that the LW model is effective for the initial stage of the liquid imbibition (10 – 20% of the equilibrium height) considering some experimental errors [34,44]. The left-hand side graphs in Fig. 14, show the magnified picture of the

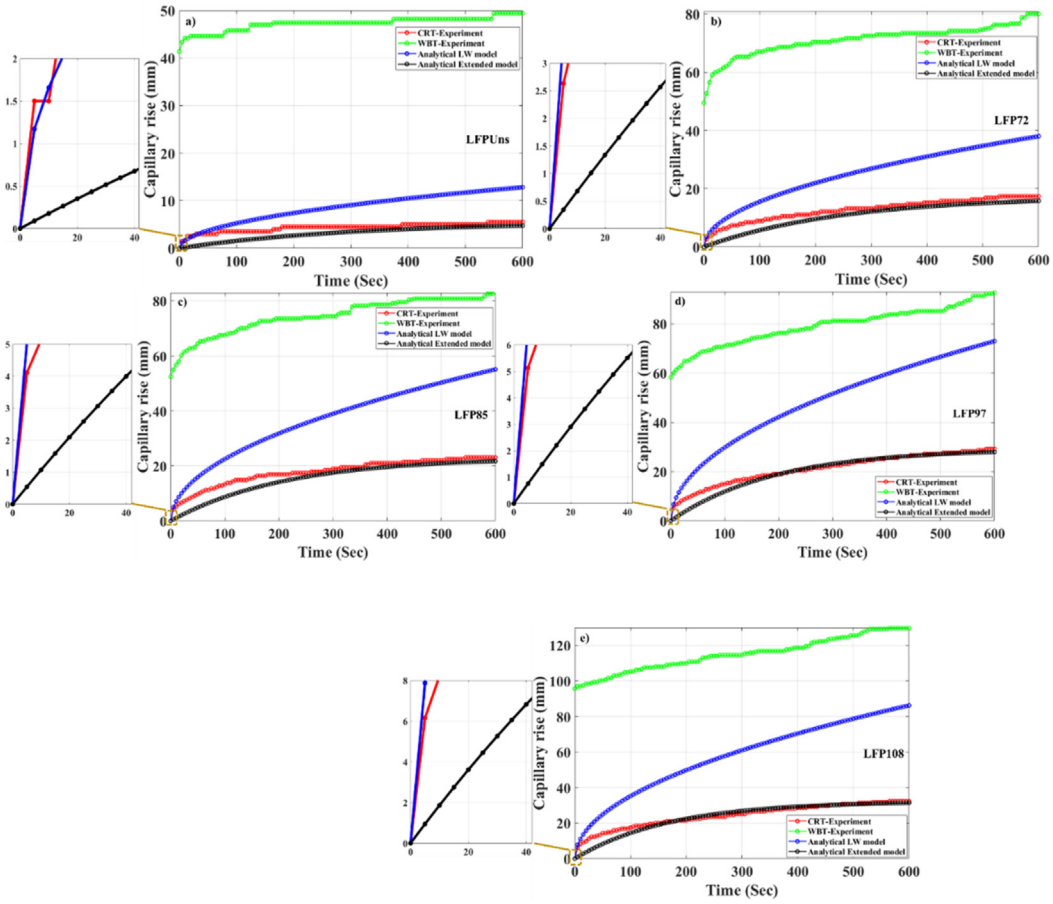


Fig. 14. LW model, extended model, and experimental results along with mark at 20% of equilibrium height a) LFPUns, b) LFP72, c) LFP85, d) LFP97, and e) LFP108.

initial periods to verify this statement. Table 9 compares the theoretical value limits where the experimental and LW model are expected to follow up together (0.1–0.2 h_{eq}). Moreover, it also contains the experimental results where these two graphs are predicting the same result (h_{expt}).

The statement in previous studies that the LW model can only predict the initial wetting stage is proved in this work's experimental result as seen in the above table. For the majority of the samples, the LW model is noticed to predict this stage with less deviation, lying in the range of 0.1–0.2 h_{eq}. These results are fairly enough to prove the statement. As discussed above the extended solution by Zhmud et al. [26](see Equation (15)) was used to compute the wetting rates quantitatively. In Fig. 15, the exact extended analytical solution provided by Fries et al. [27](see Equation (19)) is plotted along with the experiment results from both CRT and WBT, LW model, and extended Zhmud model for sample LFP108. Despite the complexity of the Fries et al. extended model, the graph indicates that this exact solution has a better capability of predicting the experimental results in the first few seconds than the asymptotic model given by Zhmud et al. Moreover, this exact solution has good agreement with LW analytical model than the extended model by Zhmud et al. However, with a longer period both extended models perform well and shows good agreement with each other as well as with the CRT experimental results.

Table 9
0.1–0.2 h_{eq} and the subsequent point where it predicts the same as the LW model (h_{expt}).

Sample	0.1–0.2 h_{eq}(mm)	h_{expt}(mm)
LFPUns	0.55–1.1	1
LFP72	1.73–3.472	2.7
LFP85	2.3–4.6	4.1
LFP97	2.92–5.84	5.1
LFP108	3.23–6.46	6.1

4.3. Electrochemical performance

Since no significant difference was observed in the wettability of LFP72, LFP85, and LFP97, the sample with a low aspect ratio which is LFP72 was used along with LFPUns and LFP108 to compare the effect of groove on the electrochemical characteristics.

4.3.1. Charge and discharge voltage profiles

The charge–discharge voltage profiles of LFPUns, LFP72, and LFP108 when cycled with 0.1C, 0.2C, 0.5C, and 1C rates are illustrated in Fig. 16 and Table 10.

The specific discharge capacity at 0.1C rate is higher for LFPUns with a discharge capacity of 148 mAh/g whereas LFP72 and LFP108 registered capacities of 144 and 142 mAh/g, respectively. LFP108 had slightly better efficiency at this C rate than the other samples despite having low relative capacity. However, samples LFP72 and LFP108 showed improvement in their coulomb efficiency as the C rate is raised to 0.5C and 1C by 4 – 6% and 35 – 40%, respectively. The discharge capacity at high C rates is mainly dependent on the transfer of electrons between particles [43]. The discharge efficiency of LFP72 and LFP108 at 0.5C is 95%, meaning that lithium ions can be free to move forth and back during the charge–discharge process. More stable performance is observed in samples LFP72 and LFP108 at low C rates, which encounter a huge decrease

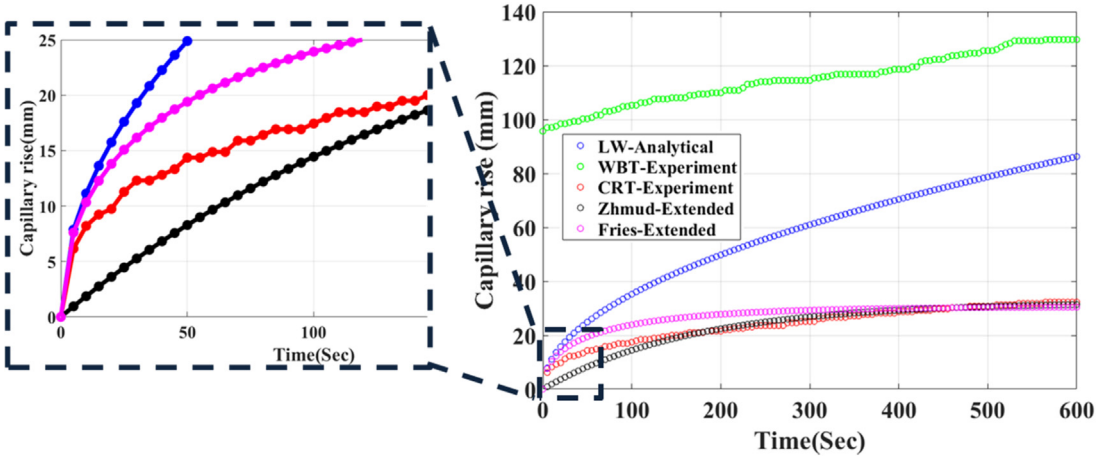


Fig. 15. LFP108 results including Fries extended model (exact extended solution).

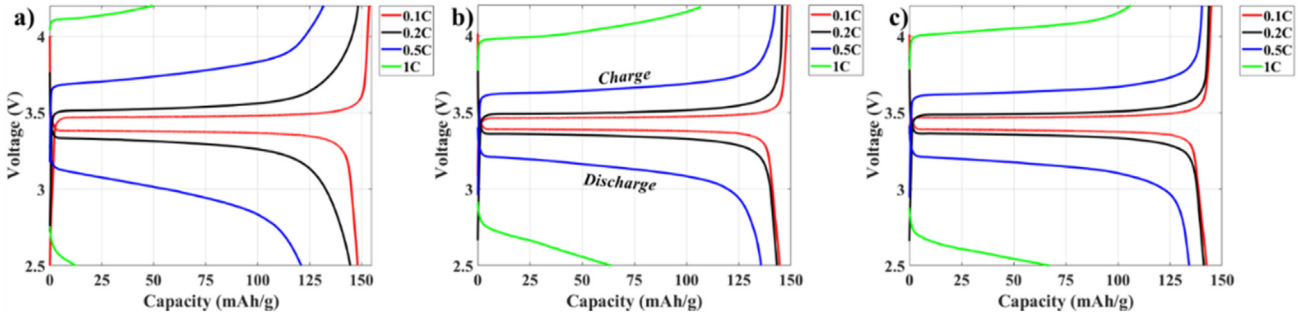


Fig. 16. Charge-discharge curves a) LFPUns, b) LFP72, and c) LFP108.

Table 10
Charge-discharge data.

	LFPUns	LFP72	LFP108
0.1C Charge capacity	153	148	145
0.1C Discharge capacity	148	144	142
0.1C Coulomb efficiency (%)	96.73	97.29	97.79
0.2C Charge capacity	148	146	143
0.2C Discharge capacity	144	143	141
0.2C Coulomb efficiency (%)	97.29	97.94	98.6
0.5C Charge capacity	131	142	140
0.5C Discharge capacity	120	135	134
0.5C Coulomb efficiency (%)	91.6	95	95.71
1C Charge capacity	49	108	106
1C Discharge capacity	12	64	67
1C Coulomb efficiency (%)	24.48	59.25	63.32

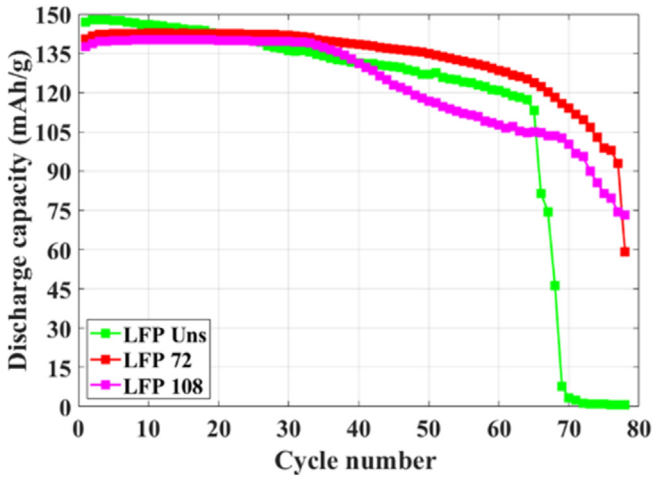


Fig. 17. Cycling stability at 0.2C rate.

when the C rate is increased. LFPUns showed a relatively huge drop every time the C rate increased, demonstrating the highest polarization [43].

4.3.2. Cyclic stability

Fig. 17 depicts the cycle performance of all samples for almost 80 cycles at a 0.2C rate. For the first 20 cycles, the capacities of LFPUns are a little higher than the other two. Despite laser structuring increasing the active surface area, the structured area will take a longer time to get wetted, which means there will be less lithium-ion diffusion resulting in less capacity in the initial cycles. High specific discharge capacity at the first cycle can be attributed to the formation of the solid electrolyte interface (SEI) film on the counter anode surface [44]. After more than 70 cycles, specific discharge capacities of 93 and 74 were achieved for LFP72 and LFP108 while LFPUns lasted only for 70 cycles. LFP72 shows stable and higher capacity while the LFPUns performed poorly for the given cycle numbers. LFP72 and LFP108 lost 34 and 46 % of their coulomb efficiency after undergoing over 70 cycles. This means specific discharge capacities of 92 mAh/g and 73 mAh/g were reached with capacity retentions of 66 and 54, respectively. This result indicates that LFP72 has a good conductive ability and improved cycling stability followed by LFP108. The rise in capacity retention is interpreted as the currents obtained from laser structured electrodes being higher than from the unstructured electrodes [6,10,21]. For lithium-ion battery cells, 80% of the initial discharge capacity is called cell-life time [8,21,46–48]. For LFPUns, this value was attained after 64 cycles reaching 117 mAh/g. For LFP72 and LFP108, they reached their cell lifetime after 71 and 60 cycles with discharge capacities of 112 and 109 mAh/g, respectively. Hence the cell lifetime is improved after laser structuring even though it is indicated that excessive removal of active material may also result in poorer performance. It is speculated that the initial specific capacities of LFPUns started falling quickly because of insufficient wetting [6,11,21,31,49].

4.3.3. Rate capability

Fig. 18 illustrates the specific charge and discharge capacities of LFPUns, LFP72, and LFP108. C rate of 0.1C was used first for the formation process, which later increased to 0.2C, 0.5C, and 1C to see the rate capability and again decreased to 0.1C to verify any possible degradation. For 0.1C, slightly less capacity is attained by LFP72 and LFP108 than by LFPUns. Cells with LFP72 and LFP108 electrodes provide improved capacities when discharged with a 0.2C rate. LFPUns decreased drastically, exhibiting capacity fading during 0.5C by dropping down to approximately 100 mAh/g (66% of initial capacity). While the other two show nearly the same performance at this C rate. Looking at 1C rate capacities, LFP72 shows excellent long-term capability. This may be due to excessive laser-induced active material mass loss for LFP108 even though LFP108 showed good wettability [10,12,50]. The impact of laser structuring is observed in higher C rates because of shorter diffusion path lengths. Meanwhile, the poor performance of unstructured electrodes is due to the complex paths through the porous electrode microstructure. After undergoing the discharging process with up to 1C rate, the C rate was finally reduced back to 0.1C. At 0.2C and 0.1C rates, less loss in discharge capacities was noticed for LFP72 and LFP108 with only a 3% drop and LFPUns possessed a 6% reduction. Thus, the cell with laser-structured electrodes showed insignificant degradation. This enhanced performance, especially in discharge capacity by the use of laser structuring mainly in LFP72 point out that there is reduced overpotential and less polarization during discharging process [22,45,48,49,50]. In addition, the laser-induced 3D structures reduce the mechanical stress compensating for the volume change during Li-ion insertion and extraction [48]. The superior rate capability of LFP72 is advantageous because lithium-ion batteries are operated in several frequently varied C rates in most applications.

Overall, the results from the laser structuring, wettability, and electrochemical tests can be summarized in Table 11.

The performance of the structured and unstructured electrodes might vary with the other publications and in some cases it might be poor. It is expected that due to the difference between purchased electrode and the materials used in the other publications

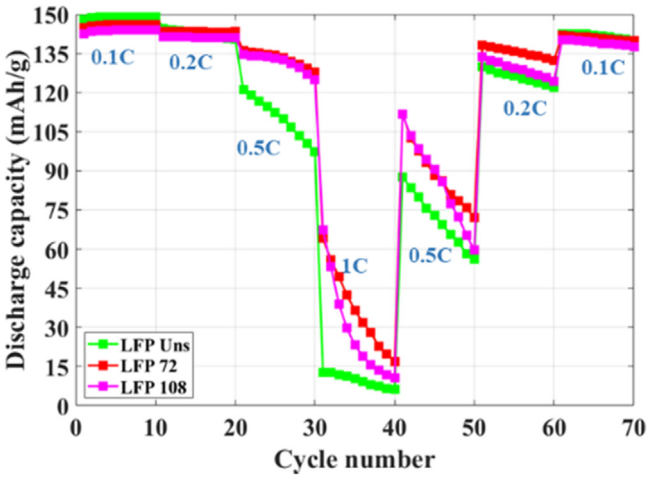


Fig. 18. Specific discharge capacity as a function of cycle number.

Table 11
Summary of results.

	Geometry	Wettability					Electrochemical performance		
	Aspect ratio	Spread area@ 5 sec (mm^2)	Wetting time (Sec)	Contact angle (°)	K_{CRT-LW} ($mm/s^{0.5}$)	K_{WBT-LW} ($mm/s^{0.5}$)	End of Life	CapacityRetention @ 0.1C (%)	Discharge Capacity @ 1C (mAh/g)
LFP108	1.08	6.02	5	17	1.44	1.57	60	97	38
LFP72	0.72	5.13	13	30	0.76	0.85	71	97	41
LFPUns	–	2.64	81	36	0.25	0.23	64	94	9

which could explain the observed variations in performance, including factors such as the manufacturing process, composition, and electrode architecture. It is widely recognized that LFP has inferior electrical conductivity compared to other cathode materials. As a result, the electrochemical performance of LFP electrodes can vary considerably depending on the degree of optimization. Therefore, even if an LFP electrode is assembled and evaluated under the same experimental conditions as other studies, it can show low performance if it has not been fully optimized. In most published papers, researchers commonly employ various methods to enhance the electrochemical performance of LFP electrodes, such as surface modification of electrode materials, carbon coating, and optimization of slurry composition. This study is focused on investigating the impact of laser structuring on the performance of the LFP electrodes and it accomplishes successfully by demonstrating enhanced electrochemical properties of structured LFPs compared to unstructured LFPs.

5. Conclusion

In this work, we have successfully demonstrated how laser structuring of electrodes can enhance the wettability and electrochemical performance of LIBs. The unprocessed electrode was structured by varying the laser power and with a detailed study of the ablation characteristics. The wettability of four sample electrodes with different aspect ratios and an unstructured electrode were investigated. The sample with a high aspect ratio (LFP108) shows improved wettability while others follow in descending order of their aspect ratio for all approaches employed to assess the wettability.

The wetting rates computed using the CRT and WBT approach with regard to the LW model provide nearly equal values. On the other hand, the wetting rate from CRT with regard to extended model had approximate value to those obtained from analytical models. It is noticed that the wetting rate obtained using the extended model was not expressive of the whole mathematical model and was unrealistic. It was found that the gravity effect is an influential force in the CRT and WBT as it balances the capillary force. It also had an impact on the wetting rate when it is taken into account. Whereas the analytical extended model shows good agreement with the CRT experimental result indicating the influence of gravity goes up as the capillary height increases. The extended model by Fries has shown its excellent predicting capability in the initial wetting time despite its complexity to extract the wetting rate quantitatively. These comparative measurement methods for wettability showed a detailed investigation of the electrolyte wetting quantitatively along with mathematical models.

The time-consuming electrolyte filling and wetting process can be improved by using laser-structured electrodes. The electrochemical performance results demonstrate that excessive active material loss by laser structuring may not improve the performance capacity regardless of a huge increase in active surface area. LFP72 electrode with a low aspect ratio showed enhanced performance, indicating that optimization of groove morphology by selecting proper laser parameters is necessary. Laser structured electrodes tend to prove that they resulted in improved capacity retention, charge–discharge capacity, and cycling performance with less cell degradation and polarization. The key parameters for improved and enhanced surface quality, wettability, and electrochemical performance have been identified in this work.

Data availability

Data will be made available on request.

Declaration of Competing Interest

The authors declare that they have no known competing financial interests or personal relationships that could have appeared to influence the work reported in this paper.

Acknowledgments

The research described herein was supported by the National Research Foundation of Korea (NRF) (No. RS-2023-00208039) funded by the Ministry of Science and ICT (MSIT, Korea), and by the "Regional Innovation Strategy (RIS) (2021RIS-004)" through the National Research Foundation of Korea (NRF) funded by the Ministry of Education (MOE, Korea). This work was also supported by the Technology Development Program (S3288700, S3275266) funded by the Ministry of SMEs and Startups (MSS, Korea), and by the Korea Institute for Advancement of Technology (KIAT) (P0018009) funded by the Ministry of Trade, Industry, and Energy (MOTIE, Korea). The opinions expressed in this paper are those of the authors and do not necessarily reflect the views of the sponsors.

References

[1] J. B. Goodenough, K. Park, "The Li-Ion Rechargeable Battery: A Perspective," 2012.
[2] B. Scrosati, J. Garche, Lithium batteries: Status, prospects and future, J. Power Sources 195 (9) (2010) 2419–2430.
[3] N. Nitta and G. Yushin, "High-Capacity Anode Materials for Lithium-Ion Batteries : Choice of Elements and Structures for Active Particles," pp. 317–336, 2014, doi: 10.1002/ppsc.201300231.
[4] B. Liang, Y. Liu, Y. Xu, Silicon-based materials as high capacity anodes for next generation lithium ion batteries, J. Power Sources 267 (2014) 469–490, https://doi.org/10.1016/j.jpowsour.2014.05.096.
[5] W. Zhang, A review of the electrochemical performance of alloy anodes for lithium-ion batteries, J. Power Sources 196 (1) (2011) 13–24, https://doi.org/10.1016/j.jpowsour.2010.07.020.
[6] W. Pfleging, R. Kohler, J. Pröll, Laser generated microstructures in tape cast electrodes for rapid electrolyte wetting: new technical approach for cost efficient battery manufacturing, Laser-based Micro- Nanoprocessing VIII 8968 (2014) 89680B, https://doi.org/10.1117/12.2039635.
[7] T. Rauscher, C.I. Müller, A. Gabler, T. Gimpel, M. Köhring, B. Kieback, W. Schade, L. Röntzsch, Femtosecond-laser structuring of Ni electrodes for highly active hydrogen evolution, Electrochim. Acta 247 (2017) 1130–1139.
[8] Z. Du, D.L. Wood, C. Daniel, S. Kalnaus, J. Li, Understanding limiting factors in thick electrode performance as applied to high energy density Li-ion batteries, J. Applied Electrochemistry. 47 (3) (2017) 405–415.

[9] J. Pröll, H. Kim, A. Piqué, H.J. Seifert, W. Pfleging, Laser-printing and femtosecond-laser structuring of LiMn2O 4 composite cathodes for Li-ion microbatteries, J. Power Sources 255 (2014) 116–124, https://doi.org/10.1016/j.jpowsour.2013.12.132.
[10] J.B. Habedank, J. Endres, P. Schmitz, M.F. Zaeh, H.P. Huber, Femtosecond laser structuring of graphite anodes for improved lithium-ion batteries: Ablation characteristics and process design, J. Laser Appl. 30 (3) (2018), https://doi.org/10.2351/1.5040611 032205.
[11] J.-H. Rakebrandt, P. Smyrek, Y. Zheng, H.J. Seifert, W. Pfleging, Laser processing of thick Li(NiMnCo)O 2 electrodes for lithium-ion batteries, Laser-based Micro- Nanoprocessing XI 10092 (2017) 100920M, https://doi.org/10.1117/12.2252093.
[12] J.B. Habedank, D. Schwab, B. Kiesbauer, M.F. Zaeh, Paving the way for industrial ultrafast laser structuring of lithium-ion battery electrodes by increasing the scanning accuracy, J. Laser Appl. 32 (2) (2020), https://doi.org/10.2351/7.0000078 022053.
[13] C.L. Cobb, M. Blanco, Modeling mass and density distribution effects on the performance of co-extruded electrodes for high energy density lithium-ion batteries, J. Power Sources 1 (249) (2014 Mar) 357–366.
[14] D. Parikh, J. Li, Bilayer hybrid graphite anodes via freeze tape casting for extreme fast charging applications, Carbon 30 (196) (2022 Aug) 525–531.
[15] S. Kalnaus, K. Livingston, W.B. Hawley, H. Wang, J. Li, Design and processing for high performance Li ion battery electrodes with double-layer structure, J. Storage Mater. 15 (44) (2021 Dec) 103582.
[16] M. Wood, J. Li, Z. Du, C. Daniel, A.R. Dunlop, B.J. Polzin, A.N. Jansen, G.K. Krumdick, D.L. Wood, Impact of secondary particle size and two-layer architectures on the high-rate performance of thick electrodes in lithium-ion battery pouch cells, J. Power Sources 515 (2021) 230429.
[17] S.J. An, J. Li, C. Daniel, D. Mohanty, S. Nagpure, D.L. Wood, The state of understanding of the lithium-ion-battery graphite solid electrolyte interphase (SEI) and its relationship to formation cycling, Carbon N. Y. 105 (Aug. 2016) 52–76, https://doi.org/10.1016/J.CARBON.2016.04.008.
[18] Y. Sheng, Investigation of Electrolyte Wetting in Lithium Ion Batteries : Effects of Electrode Pore Structures and Solution, Thesis no. December (2015).
[19] A. Davoodabadi, J. Li, H. Zhou, D.L. Wood, T.J. Singler, C. Jin, Effect of calendering and temperature on electrolyte wetting in lithium-ion battery electrodes, J. Energy Storage 26 (2019) 101034.
[20] M. Mangang, H.J. Seifert, W. Pfleging, Influence of laser pulse duration on the electrochemical performance of laser structured LiFePO4 composite electrodes, J. Power Sources 304 (2016) 24–32, https://doi.org/10.1016/j.jpowsour.2015.10.086.
[21] W. Pfleging, J. Pröll, A new approach for rapid electrolyte wetting in tape cast electrodes for lithium-ion batteries, J. Mater. Chem. A 2 (36) (2014) 14918–14926, https://doi.org/10.1039/c4ta02353f.
[22] J. Proell, R. Kohler, A. Mangang, S. Ulrich, C. Ziebert, W. Pfleging, 3D structures in battery materials, J. Laser Micro Nanoeng. 7 (1) (2012) 97–104, https://doi.org/10.2961/jlmn.2012.01.0019.
[23] R. Kohler et al., Laser-assisted structuring and modification of LiCoO 2 thin films, Laser-based Micro- Nanopackaging Assem. III 7202 (2009), https://doi.org/10.1117/12.809164 720207.
[24] R. Kohler, P. Smyrek, S. Ulrich, M. Bruns, V. Trouillet, W. Pfleging, Patterning and annealing of nanocrystalline LiCoO2 thin films, J. Optoelectron. Adv. Mater. 12 (3) (2010) 547–552.
[25] J. Pröll, R. Kohler, M. Torge, S. Ulrich, C. Ziebert, M. Bruns, H.J. Seifert, W. Pfleging, Laser microstructuring and annealing processes for lithium manganese oxide cathodes, Appl. Surf. Sci. 257 (23) (2011) 9968–9976.
[26] B.V. Zhmud, F. Tiberg, K. Hallstensson, Dynamics of capillary rise, J. Colloid Interface Sci. 228 (2) (2000) 263–269, https://doi.org/10.1006/jcis.2000.6951.
[27] N. Fries, M. Dreyer, An Analytic Solution of Capillary Rise Restrained by Gravity: online supplementary material [Online]. Available:, J. Colloid Interface Sci. 320 (2008) 259–263. http://www.zarm.uni-bremen.de/2forschung/grenzph/papers/analyticsolution2008.pdf.
[28] M.G. Berhe, D. Lee, A comparative study on the wettability of unstructured and structured lifepo4 with nanosecond pulsed fiber laser, Micromachines 12 (5) (2021) 1–9, https://doi.org/10.3390/mi12050582.
[29] Y. Sheng, C.R. Fell, Y.K. Son, B.M. Metz, J. Jiang, B.C. Church, Effect of calendering on electrode wettability in lithium-ion batteries, Front. Energy Res. vol. 2 (DEC) (2014) 1–8, https://doi.org/10.3389/fenrg.2014.00056.
[30] W. Gardner, Note on the dynamics of capillary flow, Phys. Rev. 18 (3) (1921) 206–209, https://doi.org/10.1103/PhysRev.18.206.
[31] N. Fries, M. Dreyer, An analytic solution of capillary rise restrained by gravity, J. Colloid Interface Sci. 320 (1) (2008) 259–263, https://doi.org/10.1016/j.jcis.2008.01.009.
[32] N. Fries, Capillary transport processes in porous materials - experiment and model. 2010.
[33] T.P. Dence, A brief look into the Lambert W function, Appl. Math. 2013 (4) (2013) 887–892.
[34] J. Pröll et al., Laser modification and characterization of Li-Mn-O thin film cathodes for lithium-ion batteries, Laser-based Micro- Nanopackaging Assem. V 7921 (2011) 79210Q, https://doi.org/10.1117/12.873700.
[35] M. Mangang, J. Pröll, C. Tarde, H.J. Seifert, W. Pfleging, Ultrafast laser microstructuring of LiFePO 4 cathode material, Laser-based Micro-Nanoprocessing VIII 8968 (2014) 89680M, https://doi.org/10.1117/12.2039604.
[36] A. Davoodabadi, J. Li, Y. Liang, D.L. Wood, T.J. Singler, C. Jin, Analysis of electrolyte imbibition through lithium-ion battery electrodes, J. Power Sources 424 (April) (2019) 193–203, https://doi.org/10.1016/j.jpowsour.2019.03.115.
[37] T. Liu, K. Wang, Y. Chen, S. Zhao, Y. Han, Dominant role of wettability in improving the specific capacitance, Green Energy Environ. 4 (2) (2019) 171–179, https://doi.org/10.1016/j.gee.2019.01.010.
[38] M.S. Wu, T.L. Liao, Y.Y. Wang, C.C. Wan, Assessment of the wettability of porous electrodes for lithium-ion batteries, J. Appl. Electrochem. 34 (8) (2004) 797–805, https://doi.org/10.1023/B:JACH.0000035599.56679.15.
[39] G. Bamorovat Abadi, M. Bahrami, A general form of capillary rise equation in micro-grooves, Sci. Rep. 10 (1) (2020) 1–11, https://doi.org/10.1038/s41598-020-76682-2.
[40] V.R. Lucas, Cleber das Zeitgesetz des kapillaren P, ufstiegs yon Fliissigkeiten, Kolloid-Zeitschrift 23 (1) (1918) 15–22.
[41] C.H. Choi, S. Krishnan, W. TeGrotenhuis, C.H. Chang, Capillary rise of nanostructured microwicks, Micromachines 9 (4) (2018) 1–14, https://doi.org/10.3390/mi9040153.
[42] S. Benltoufa, F. Fayala, S. BenNasrallah, "Capillary Rise in Macro and Micro Pores of Jersey Knitting Structure," J. Eng. Fiber. Fabr., vol. 3, no. 3, p. 155892500800300, 2008, doi: 10.1177/155892500800300305.
[43] L. Chen, Z. Chen, S. Liu, H. Zhang, Q. Huang, Study on highly compacted LiFePO4 / C cathode materials for high-performance 18650 Li-ion batteries, Int. J. Electrochem. Sci. 13 (6) (2018) 5413–5424, https://doi.org/10.20964/2018.06.21.
[44] Y. Zheng and H. J. Seifert, "Development of Laser Structured Silicon-based Anodes for Lithium-ion Batteries," pp. 2018–2021, 2018.
[45] W. Pfleging, Y. Zheng, M. Mangang, M. Bruns, P. Smyrek, Laser processes and analytics for high power 3D battery materials, Front. Ultrafast Opt. Biomed. Sci. Ind. Appl. XVI, vol. 9740 (2016), https://doi.org/10.1117/12.2212041 974013.
[46] W. Pfleging, M. Mangang, Y. Zheng, P. Smyrek, Laser structuring for improved battery performance, SPIE Newsroom 1 (2016) 10–12, https://doi.org/10.1117/2.1201602.006342.
[47] M. Mangang, H. J. Seifert, and W. P, "In fl uence of laser pulse duration on the electrochemical performance of laser structured LiFePO 4 composite electrodes," vol. 304, pp. 24–32, 2016, doi: 10.1016/j.jpowsour.2015.10.086.
[48] Y. Zheng and P. Smyrek, "Lithium-ion Battery," vol. c, no. Vc, pp. 5–8.
[49] J. Park, S. Hyeon, S. Jeong, H.J. Kim, Performance enhancement of Li-ion battery by laser structuring of thick electrode with low porosity, J. Ind. Eng. Chem. 70 (2019) 178–185, https://doi.org/10.1016/j.jiec.2018.10.012.
[50] R. Kohler, J. Proell, H. Besser, M. Torge, S. Scholz, T. Dobrev, S. Ulrich, W. Pfleging, Nanosecond and picosecond laser structuring of electrode materials for lithium-ion batteries, MRS Proc. 1388 (2012), https://doi.org/10.1557/opl.2012.1174.
[51] J. Li, C. Rulison, J. Kiggans, C. Daniel, D.L. Wood, Superior performance of LiFePO4 aqueous dispersions via corona treatment and surface energy optimization, J. Electrochem. Soc. 159 (8) (2012) A1152–A1157.
[52] A. Davoodabadi, J. Li, Y. Liang, R. Wang, H. Zhou, D. Wood, T.J. Singler, C. Jin, Characterization of surface free energy of composite electrodes for lithium-ion batteries, J. Electrochem. Soc. 165 (11) (2018) A2493–A2501.